LOW TEMPERATURE – HIGH MAGNETIC FIELD PHASE DIAGRRAM OF $CeRhIn_5$ MEASURED BY THERMAL EXPANSION AND LINEAR MAGNETOSTRICTION

E. W. Okraku [1], V. F. Correa [2]
[1] Occidental College, Los Angeles, California 90041
[2] Los Alamos National Laboratory, New Mexico 87545

We report linear thermal-expansion and linear magnetostriction results on the newly discovered $CeRhIn_5$ at low temperatures and high magnetic field. For fields applied along the crystallographic a-axis, the magnetic field versus temperature phase diagram is very rich in agreement with previous specific heat data. First and second order phase transition were clearly observed in linear magnetostriction measurements.

INTRODUCTION

$CeRhIn_5$ is a member of a larger group of strongly correlated-electron systems often referred to as heavy fermions. It has a tetragonal structure, with alternating layers of $CeIn_3$ and $RhIn_2$ as shown in Fig 1a. The magnetic moments of the Ce atoms order antiferromagnetically at T_N =3.8K. In this ordered state the moments lie in the basal plane (001) developing a helicoidal structure along the c-axis as seen in Fig 1b.[1] Specific heat experiments for fields applied along the crystallographic a-axis show several transitions resulting in a rich magnetic field versus temperature phase diagram.[2] In this work, we report low temperature(down to 1.4K) high magnetic field (up to 18T) linear thermal-expansion and linear magnetostricition results for $CeRhIn_5$ single crystals. A rich B-T phase diagram is obtained when B is parralel to the crystallographic basal plane in agreement with specific heat data.

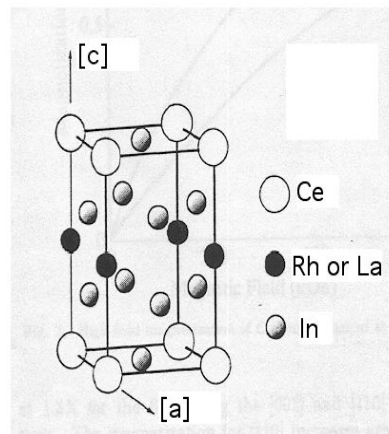

Fig 1a: Crystal structure of *$CeRhIn_5$*

Fig 1b: Magnetic structure below T_N

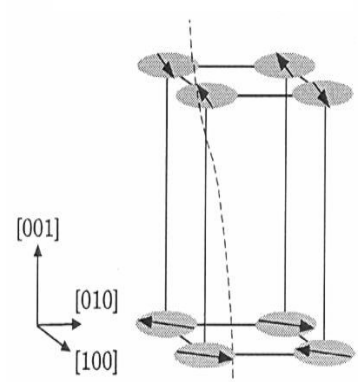

EXPERIMENTAL DETAILS.

X-ray diffraction methods are employed to determine the crystallographic axes of the compound . Linear thermal expansion measurements are taken along both the a-axes and the c-axis at constant magnetic fields. Likewise, at constant temperature, linear magnetostiction measurements are taken. A 20T superconductor magnet was used with the cryogenic liquid nitrogen kept at 77K and the helium at 4.2K. Linear thermal expansion or linear magnetostriction measurements were taken with an Oxygen-Free High-Conductivity (OFHC) copper capacitance dilatometer with known expansion specifications.

Section I: X-ray diffraction-finding the c and a-axes.

The sample had been cut and trimmed to have the surface flush with the crystallographic axes. X-ray experiments were performed to distinguish between the a-axis and c-axis and to see if the sample was truly a single crystal. Using Bragg's relation ($n\lambda = 2d\sin\theta$) where d is the distance between the lattice planes, λ is the wavelengh of the incident beam with well-known values of the distance between the lattices d (d_A=0.4652nm and d_C=0.7542nm), the incident angles at which constructive interference patterns occur can be determined. For the a-axis, the contructive interference occurs at approximately 2θ=19.1°. In our sample, the

constructive interference occurred at 2θ=19.2°. Likewise the contructive interference for measurements along the c-axis was expected to be at 2θ=35° and 2θ=48.5° and the data from our measurements correspond approximately.

Figures 2a and 2b below show the intensity of the x-ray interference at different incident angles. The diffraction patterns produced help identify the approximate a and c- axes and confirm the single crystal quality of the sample.

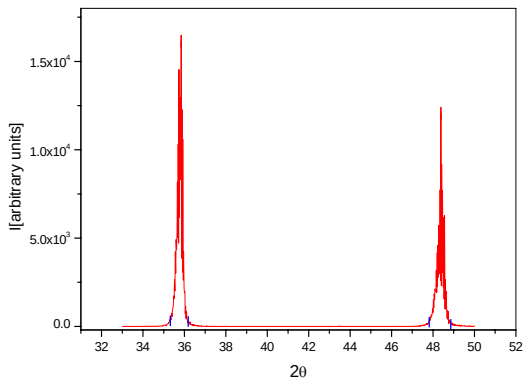

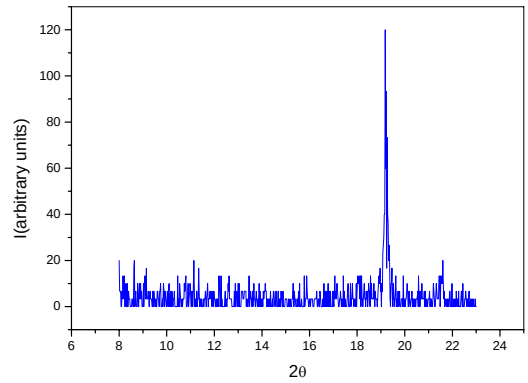

Fig. 2a **Fig. 2b**

Figure 2a shows the x-ray diffraction pattern for the c-axis of the sample. Notice the peaks at 35.5 ° and 48.5° . Figure 2b shows a different x-ray diffraction pattern for the the a--axis. Notice the peak at 19°.

Section II: Linear Therma-Expansion and Linear magnetostriction.

Thermal-expansion and linear magnetostriction measurements were done in an OFHC copper cell (shown below Fig 4) The cell is contained in a double dewar cryostat with a Nitrogen dewar on the outside followed by a Helium dewar (shown in Figure 3 below). The VTI (Variable Temperature Insert) or experimental insert is in the innermost section of the cryostat and holds the probe. A little outlet in the VTI allows helium to flow around the probe and control the temperature. The VTI is placed in a superconducting magnet made as a solenoid as shown in figure 3 below.

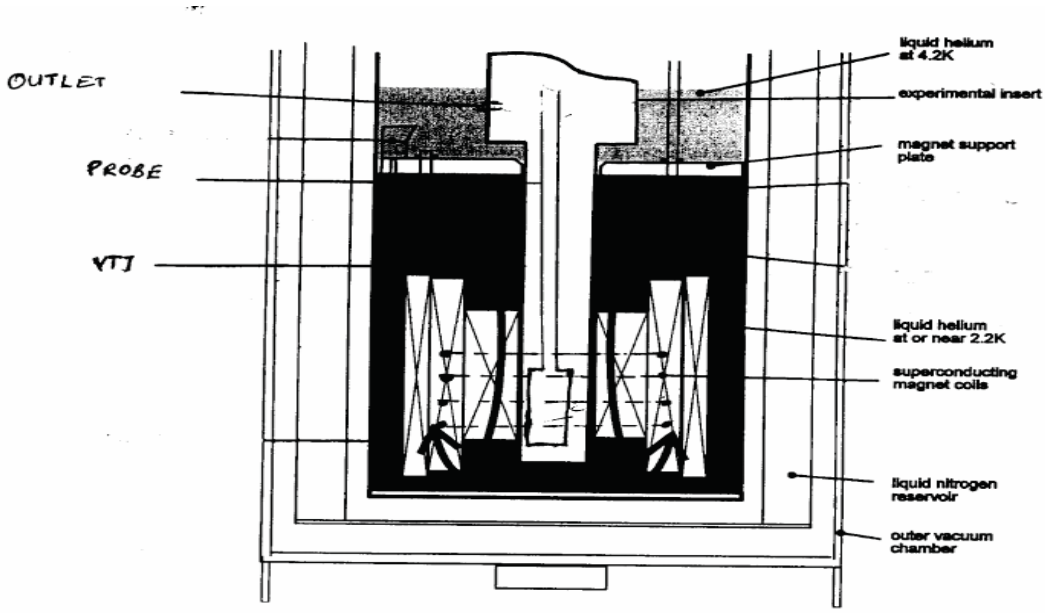

Fig. 3 Cross-section of apparatus used showing superconducting magnet, and probe.

The OFHC cell at the bottom of the probe holds the sample. As shown in figure 4, the sample is placed beneath the parallel plates of a capacitor. The sample is in contact with the lower plate of the capacitor. Changes in the length of the sample change the distance between the two plates and hence the capacitance. The capacitance is recorded and converted to distances using the infinite parralel plate capacitor relationship ,

$$C = \frac{\varepsilon_0 A,}{d}$$

where C is the capacitance , ε_o is the vacumm permitivity, A is the surface area of the plates and d is the distance between the two plates.

During thermal expansion measurements, the cell expands as well as the sample. As such , we have to account for this cell effect. To do this, an OFHC copper sample which has universally known linear thermal expansion data is placed in the cell. .

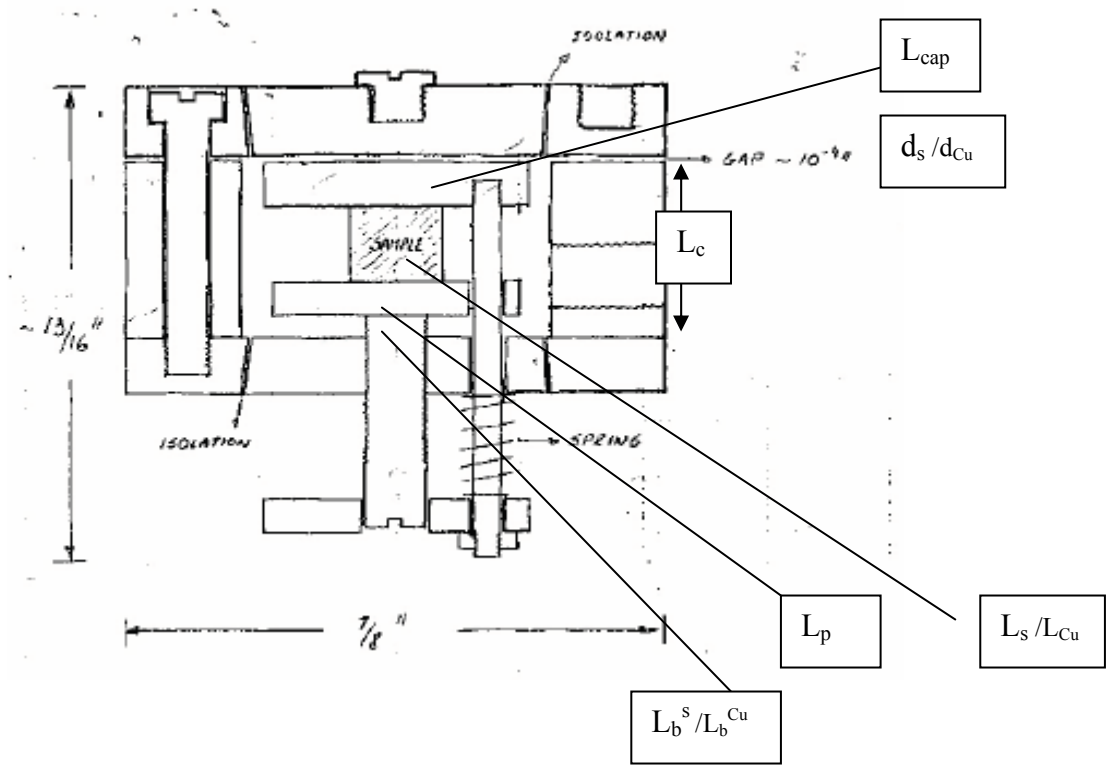

Fig.4.OFHC cell containing sample to demostrate steps in finding the relationship for linear themal expansion coefficient.

Considering the diagram above, the cell has the same total length L_c regardless of whether it contains the sample or a piece of copper.

For the cell containing the sample ,

$$L_c = L_b^S + L_p + L_{Cap} + d_{Cu}$$

and the cell with the copper sample

$$L_c = L_b^{Cu} + L_p + L_{Cu} + L_{cap} + d_{Cu}$$

Since the total length of the cell Lc is the same regardless of the sample in place, the two relationships are the same and equating then to each other give

$$L_s = L_b^{cu} + L_{Cu} + d_{Cu} - L_b^s - d_s$$

Hence, we find that

$$\frac{1}{L_s}\frac{\partial L_s}{\partial T} = \frac{1}{L_s}\frac{\partial(L_b^{cu} + L_{Cu} + d_{Cu} - L_b^s - d_s)}{\partial T}$$

Since

$$\alpha_s = \frac{1}{L_s}\frac{\partial L_s}{\partial T}$$

then,

$$\alpha_s = \frac{1}{L_s}\left(\frac{L_b^{Cu}}{L_b^{Cu}}\frac{\partial L_b^{Cu}}{\partial T} + \frac{L_{Cu}}{L_{Cu}}\frac{\partial L_{Cu}}{\partial T} + \frac{\partial d_{Cu}}{\partial T} - \frac{L_b^s}{L_b^s}\frac{\partial L_b^s}{\partial T} - \frac{\partial d_s}{\partial T}\right)$$

and likewise

$$\frac{1}{L_b^{Cu}}\frac{\partial L_b^{Cu}}{\partial T} = \frac{1}{L_{Cu}}\frac{\partial L_{Cu}}{\partial T} = \frac{1}{L_b^s}\frac{\partial L_b^s}{\partial T} = \alpha_{Cu}$$

since L_b^{Cu}, L_{Cu} and L_b^s are pieces of the cryostat made of copper. As such

$$\alpha_s = \frac{1}{L_s}\left(L_b^{Cu} + L_{Cu} - L_b^s\right)\alpha_{Cu} + \frac{1}{L_s}\left(\frac{\partial d_{Cu}}{\partial T} - \frac{\partial d_s}{\partial T}\right)$$

From above ,

$$L_b^{Cu} + L_{Cu} - L_b^s = L_s + d_s - d_{Cu}$$

and $d_s \approx d_{Cu}$

So,

$$\alpha_s \approx \alpha_{Cu} + \frac{1}{L_s}\left(\frac{\partial d_{Cu}}{\partial T} - \frac{\partial d_s}{\partial T}\right)$$

Above is the linear thermal-expansion relation accounting for the cell effect. In previous experiments, $\frac{\partial d_{Cu}}{\partial T}$ had been determined. The length along the a-axis was 1.32 mm and along the c-axis was 1.82mm for the $CeRhIn_5$ sample and α_{Cu} is universally known . The capacitance was measured with an Andeen Haagerling capacitance bridge with an accuracy of 10^{-6} pF. This transforms to an accuracy of 1Å in measuring the thermal expansion($\Delta d = \varepsilon_o A\Delta C/C^2$). The temperature was measured with a sensor attached to the lower plate of the capacitor.

RESULTS.

Fig 5 below shows the anisotropic behavior of the linear thermal expansion coefficent along the c-axis and a-axis at 0T.

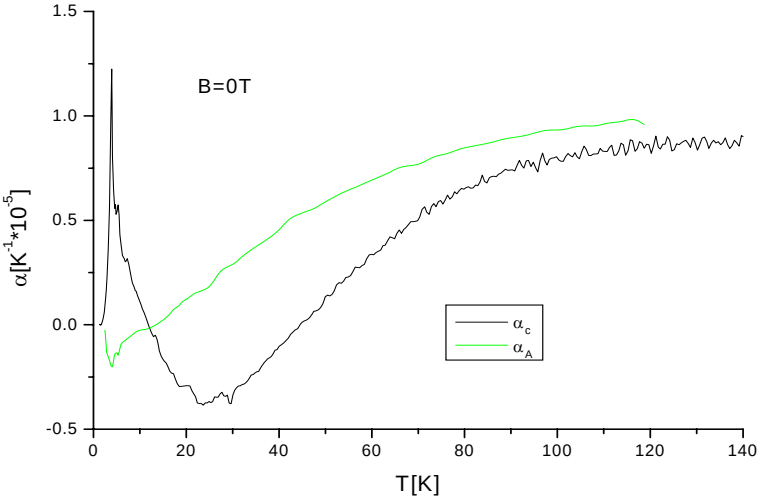

Figure 5:comparing linear thermal expansion coefficient measurements along the a and c axes at 0T.

At high temperatures the thermal expansion coefficient tends to be independent of temperature. However, at low temperatures, the linear coefficient becomes temperature dependent. Two interesting behavior can be observed: the peak in the linear thermal expansion coefficient around 4K associated with the antiferromagnetic transition and the negative c-axis linear thermal expansion coefficient between 20-40K due to crystal electric field (CEF) effects.

Magnetostriction is the volume dependence on magnetic field. It is caused by the re-orientation of the magnetic moments in the presence of a magnetic field especially for compounds with strong spin-orbit coupling. The linear magnetostriction coefficient by definition is

$$\lambda = \frac{\Delta L_s}{L_s}$$

Unlike for the sample, magnetic fields do not cause significant volumetric changes in the OFHC copper. This is because the spin-orbit coupling in copper is very weak, and the mean orbital angular momentum of copper is approximately zero. As such the linear magnetostriction of the sample does not need to be corrected for the expansion of the copper cell. Fig. 6 below shows the linear magnetostriction co-efficient for varying fields along the a-axis at 1.7K and 3.75K.

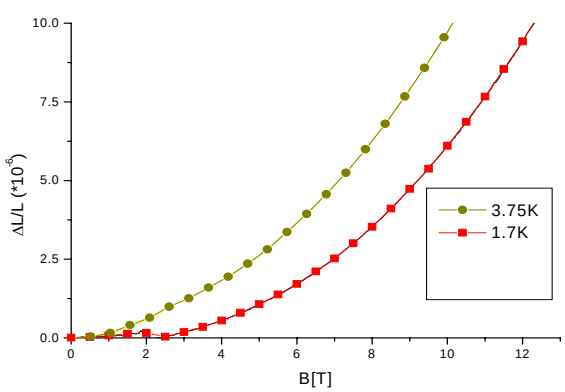

Fig. 6 shows linear magnetostriction data for magnetic field strengths between 0 and 12T for 1.7K and 3.75K

For our sample the linear magnetostriction is also anisotropic (not shown in fig above). The field dependence of $\Delta L_s/L_s$ increases with temperature in the low T region. This anomalous behavior was already reported by Malinowski *et al.* in the analog Ce_2RhIn_8 and was ascribed to the magnetic correlations.[3]

Section IV: Discussion.

According to the Heisenberg model, the energy between two adjacent magnetic moments is given by

$$E_M = j\, \mu_1 \bullet \mu_2$$

where j is a constant and μ_1 and μ_2 are two adjacent magnetic moments. For our compound, j is positive. Since at low temperature and in the absence of significant magnetic fields, the dominant energy is the energy between the moments, the total energy of the system will be minimized by reducing this energy. As such, adjacent moments are ordered in opposite directions to minimize the total energy. This state is which adjacent moments point in opposite directions is the antiferromagnetic state.

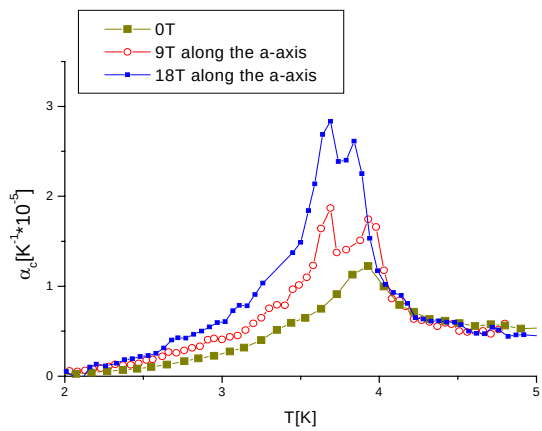

Fig. 7a

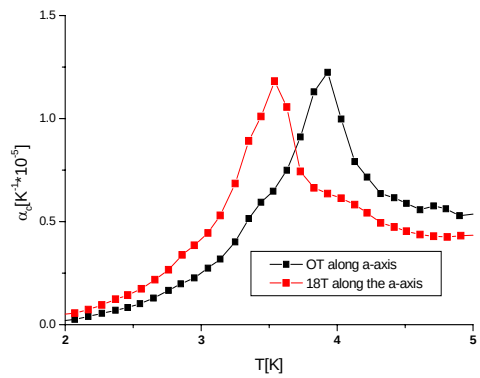

Fig. 7b

Fig 7a. shows low temperature linear thermal-expansion for fields applied along the a-axis (fig 7a) and the c-axis (fig 7a). In the first, two transtions are observed at finite fields.

Figure 7a shows the linear thermal-expansion coefficient versus temperature in the region around the Néel temperature (2-5K) when a field is applied along the a-axis. In figure 7b, we present the linear thermal-expansion coefficient versus temperature for a field applied to the c-axis in the 2-5K region. Firstly, we observe a double peak representing two transitions only when a field is applied along the a-axis and a single peak when a field is applied towards the c-axis. In fig 7b, the linear thermal expansion coefficient at the Néel temperature for an 18T field along the c-axis, is approximately the same as the linear thermal expansion coefficient at the Néel temperature for 0T. This implies that the 18T field along the c-axis has an almost negligible contribution to the re-orientation of the magnetic moments at the Néel temperature and suggests that the field was perpendicular to the moments, that is, the moments lie in the ab-plane. In analyzing fig 7a, we observe that at temperatures above 4K, the linear thermal expansion coefficient is independent of the magnetic field applied along the a-axis. However, at temperatures below 4K, the Néel temperature is strongly field dependent: they are lower for stronger magnetic fields along the a-axis. In addition, the linear thermal expansion coefficient is higher at the Néel temperature for stronger magnetic fields applied along the a-axis. This can be attributed to changing magnetic moment orientation, and suggests also that the moments lie in the ab-plane which agrees with the results from W. Bao *et al.*[4]

As the temperature is increased above the Neel temperature, the compound reaches equilibrium where the thermal energy equals the energy between the magnetic moments. With further increases in the thermal energy, the entropic effect dominates the free energy and the system becomes disordered, that is , the paramagnetic phase.

Consider the relation

$$E_m = -\mu \bullet B$$

where E_m is the magnetic energy, μ is the magnetic moment and is B is the magnetic field. The magnetic energy is minimized when all the magnetic moment are in the same direction as the magnetic field. Thus, all the magnetic moments point in the same direction in the initial stages of the paramagnetic phase.

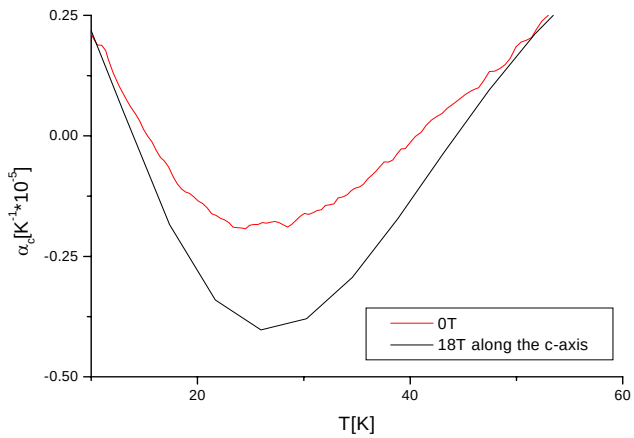

Fig.8 shows the dependence of the linear thermal expansion coefficient on the magnetic field in the region of approx. 10-60K.

Figure 8 shows the linear thermal-expansion coefficient versus temperature for 0T and 18T fields applied along the c-axis in the 15K to 60K temperature range. In the absence of significant magnetic fields, the six different m_J states of the J = 5/2 Ce^{3+} multiplet are arranged in three doublets (CEF effect). As the temperature is raised, the population of the excited doublet states introduces a negative extra contribution to the c-axis thermal-expansion as was previously reported.[5] In the presence of strong magnetic fields, the Zeeman Effect occurs: magnetic fields break the degeneracy completely into all six m_J - states. The energy difference between the states is proportional to the magnetic field strength. As a result, a field dependent thermal-expansion coefficient is observed at the 15K to 60K range.

At higher temperatures (above 60K), the classical constant value limit due to the atomic lattice vibrations is reached.

Section IV: Orders of Phase transition

In our linear thermal-expansion and linear magnetostriction measurements we noted two orders of phase transitions: first and second order phase transition. By definition, the first derivatives of the Gibbs free energy relation give us the first orders of the phase transition. Considering the Gibbs Free Energy relation,

$$G = G(T,P,B)$$

where T is the temperature, P is the pressure and B is the magnetic field, the first order derivative of this relationship is,

$$dG = \left.\frac{\partial G}{\partial T}\right)_{P,B} dT + \left.\frac{\partial G}{\partial P}\right)_{T,B} dP + \left.\frac{\partial G}{\partial B}\right)_{T,P} dB = -SdT + VdP + MdB$$

For our purposes, two important second order derivatives are

$$\alpha = \frac{1}{V}\left.\frac{\partial V}{\partial T}\right)_{P,B} \quad \text{and} \quad \left.\frac{\partial G}{\partial P \partial B}\right)_{T,P} = \left.\frac{\partial V}{\partial B}\right)_{T,P}$$

First order transitions occur when the first derivatives of the Gibbs free energy are discontinuous, or when we observe peaks in the second order derivatives. Similarly, second order transitions are defined as discontinuities in the second derivatives of the Gibbs free energy.

The peaks observed in the linear thermal-expansion coefficient measurements are second order transitions. However, in the linear magnetostriction measurements, we observed both first and second order

transitions. Fig. 9a shows a discontinuity in the linear magnetostriction measurements at 1.59K associated with a first order pahse transition.

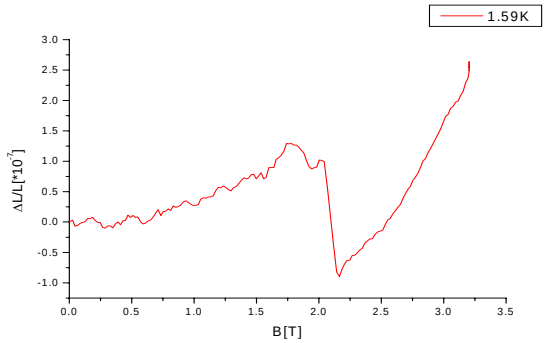

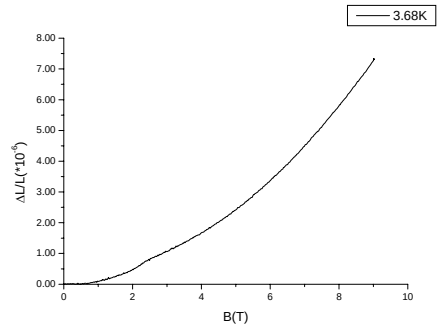

Figure 9a shows the first order transition derived from transtions linear magnetostriction measurements at 1.59K

Figure 9b shows the second order taken from linear magnetostriction measurements.

Fig 9b. above shows a second order transition at approximately 2.5T from linear magnetostriction measurements.

The transition points from both linear magnetostriction and linear thermal expansion data was collected. Plotting out the different transition points presents the phase diagram below.(Fig 10)

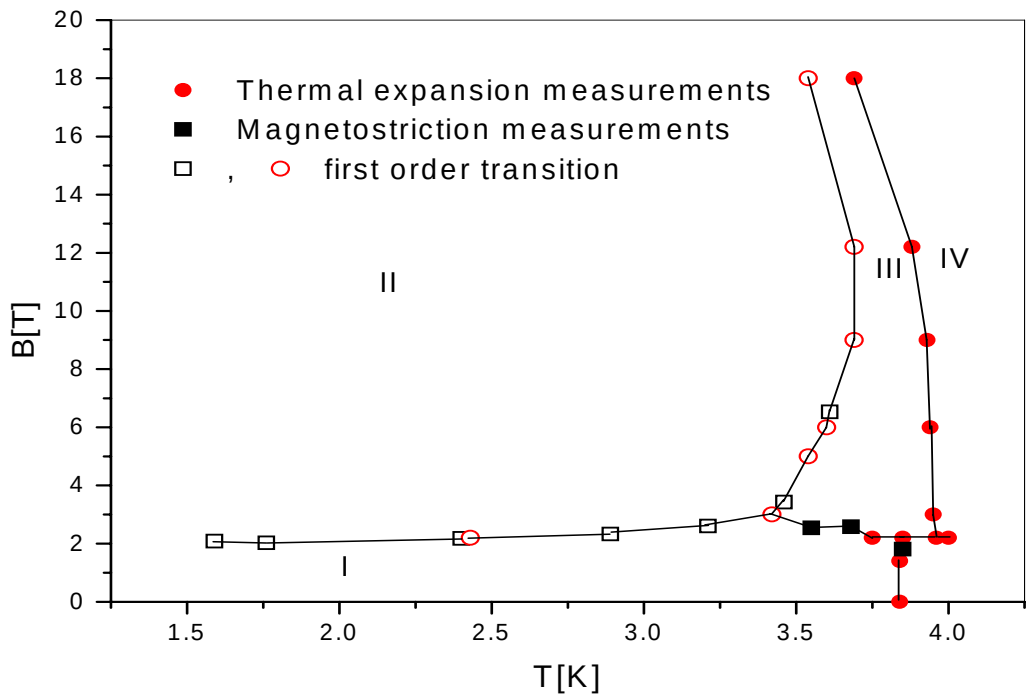

Figure 10 shows the low temperature-high magnetic field phase diagram for *CeRhIn$_5$*. Data for the diagram was obtained using linear magnetostriction and thermal expansion measurements. Hollow symbols represent first order transitions.

Section V :Conclusion and Acknowledgement.

The low temperature-high magnetic field phase daigram of *CeRhIn$_5$* we obtained using linear thermal expansion and linear magnetostriction measurements matches perfectly with the phase diagram produced by A.L Cornelius through specific heat experiments. In addition, we observe distinct anisotropic behavior

in the linear thermal expansion coefficient and linear magnetostriction measurements along both axes. Measurements with fields applied towards the crystallographic a-axis produced a very rich phase diagram.

Since there is a first order phase transition between phases I and II (as shown on fig 10 above), a logical extension will be to investigate if structural phase transitions can be induced by magnetic fields in the compound. Luckily, this is an ongoing project at the National High Magnetic Field Laboratiory (NHMFL) at Los Alamos National Laboratory. Resonant ultra-sound techniques will be used to trace the changes in the elastic constants as the field is increased from regime I to II (refer to fig. 10).

This project was done as part of Dr. Victor Correa's post-doctorial work at Los Alamos Nat. Lab. Many thanks to him and the management of the NHMFL at Los Alamos and Tallahassee.

References

1.T. Takeuchi, T Inoue, K Sugiyama e*t al*. : Phys. Soc. Jpn **70** 881 (2001)
2.A. Cornelius, Phys. Rev. B **64** 144411 (2001)
3.A. Malinowiski *et al.* :Phys. Rev B **68** 184419 (2003)
4.W. Bao *et al.* : Phys. Rev. B **62** R14621 (2000)
5. V. Correa *et al.* : Phys. Rev. B **69** 174424 (2004)